PROCEEDINGS A

royalsocietypublishing.org/journal/rspa

Research

Cite this article: Durey M, Turton SE, Bush JWM. 2020 Speed oscillations in classical pilot-wave dynamics. *Proc. R. Soc. A* **476**: 20190884.
http://dx.doi.org/10.1098/rspa.2019.0884

Received: 18 December 2019
Accepted: 24 June 2020

Subject Areas:
applied mathematics

Keywords:
pilot-wave theory, emergent statistics, statistical structure, self-propelled particles, chaos and nonlinear dynamics

Author for correspondence:
John Bush
e-mail: bush@math.mit.edu

Electronic supplementary material is available online at https://doi.org/10.6084/m9.figshare.c.5053418.

THE ROYAL SOCIETY PUBLISHING

Speed oscillations in classical pilot-wave dynamics

Matthew Durey, Sam E. Turton and John W. M. Bush

Department of Mathematics, Massachusetts Institute of Technology, Cambridge, MA 02139, USA

MD, 0000-0002-4232-1705

We present the results of a theoretical investigation of a dynamical system consisting of a particle self-propelling through a resonant interaction with its own quasi-monochromatic pilot-wave field. We rationalize two distinct mechanisms, arising in different regions of parameter space, that may lead to a wavelike statistical signature with the pilot-wavelength. First, resonant speed oscillations with the wavelength of the guiding wave may arise when the particle is perturbed from its steady self-propelling state. Second, a random-walk-like motion may set in when the decay rate of the pilot-wave field is sufficiently small. The implications for the emergent statistics in classical pilot-wave systems are discussed.

1. Introduction

Louis de Broglie [1–3] proposed a physical picture of quantum dynamics according to which microscopic quantum particles move in resonance with a guiding wave field centred on the particle and generated by its internal vibration. For a particle of rest mass m, the frequency of internal vibration was posited to be the Compton frequency, ω_c, as follows from the Einstein-de Broglie relation, $mc^2 = \hbar\omega_c$, where c is the speed of light and $\hbar$ is the reduced Planck constant. The resonance between particle and wave, which de Broglie referred to as the 'harmony of phases', insured that the guiding or 'pilot' wave be synchronized with the particle vibration in all frames of reference. The particle was posited to move along a line of constant phase of its pilot-wave field, from which follows the de Broglie relation for the particle momentum, $\boldsymbol{p} = \hbar\boldsymbol{k}_B$, for a monochromatic wave with wavevector $\boldsymbol{k}_B$. This physical picture of 'matter waves' was instrumental in the development of the mathematical framework of quantum mechanics: not only did it bear fruit in the form of the Einstein-de Broglie and de Broglie relations, but it motivated

Schrödinger's derivation of both the Klein–Gordon and Schrödinger equations to describe the evolution of the guiding wave [4]. Moreover, it led de Broglie to predict single-particle diffraction, the experimental confirmation of which resulted in de Broglie's Nobel prize in 1929. Nevertheless, it was soon superseded by the Copenhagen Interpretation, which furnishes no accompanying physical picture for the quantum realm [5]. Attempts to do so have included Nelson's stochastic dynamics [6], according to which quantum mechanics may be seen as a diffusive process with diffusivity $\mathcal{D}_0 = \hbar/(2m)$. In different parameter regimes, the classical pilot-wave system considered here will exhibit features of both de Broglie's and Nelson's mechanics.

At the time that de Broglie proposed his pilot-wave theory of quantum dynamics, there was no macroscopic analogue from which to draw physical insight. Some 90 years later, a hydrodynamic pilot-wave system was discovered by Yves Couder and Emmanuel Fort [7–9]. It takes the form of a millimetric fluid droplet bouncing on the surface of a vibrating fluid bath, walking in resonance with its quasi-monochromatic Faraday pilot-wave field. Notably, the pilot wave in this system possesses two key ingredients of de Broglie's mechanics; resonance between the droplet and its pilot wave, and a quasi-monochromatic wave field [10]. The droplet is dressed in a spatially extended wave field, and exhibits several features previously thought to be exclusive to the microscopic quantum realm [10,11]. Central to the 'walker' dynamics is the notion of path memory [9]: the wave force imparted to the walker depends on the pilot-wave field generated by its previous bounces. The droplet's history thus affects the local wave potential acting on it. The more long-lived its waves, the longer its path memory. The droplet dynamics is explicitly non-local in time: prediction of the walker's future requires knowledge not only of its present state but also of its past. Furthermore, the non-Markovian nature of the dynamics may lead to the misinference of spatially non-local effects in the droplet motion. For example, in considering the interaction between a walker and a submerged pillar [12] or well [13], if the influence of the pilot-wave field is not taken into account, one might infer action at a distance [11].

While the walking-droplet system is the first macroscopic realization of a pilot-wave dynamics of the form proposed by de Broglie, its limitations as a quantum analogue prompted Bush [10] to propose the exploration of the parametric generalization of the stroboscopic trajectory equation developed by Oza *et al.* [14] to describe the dynamics of walking droplets. This generalized pilot-wave framework provides a means of exploring a new class of classical dynamical systems in which the key features of pilot-wave dynamics are retained, specifically, wave-particle resonance and a quasi-monochromatic pilot-wave field, while the limitations of the hydrodynamic system may be side-stepped. This theoretical framework has since been shown to exhibit a rich class of new dynamical behaviours. For example, it has revealed a parameter regime, beyond that accessible in the laboratory [15], in which hydrodynamic spin states (characterized by the circular motion of a walking droplet radially confined by its own wave field) are stable [16]. It also revealed a parameter regime in which a particle orbiting in an oscillatory potential (with the form of a Bessel function) may achieve a statistically steady state characterized by intermittent switching between unstable circular orbits [17]. The same framework was adopted by Valani & Slim [18], who discovered an abundance of exotic dynamical states for two interacting walkers.

The walking-droplet system has provided three distinct paradigms for the emergence of quantum-like statistics from classical pilot-wave dynamics. The first such paradigm was revealed through studies of orbital pilot-wave dynamics, in which the walker motion is constrained by an imposed external force [11]. In such systems, the quasi-monochromatic pilot-wave field imposes a dynamical constraint on the droplet motion, the result being the preference for a discrete number of quantized periodic orbital states [19–24]. In the chaotic regime arising in the long-path-memory limit, the system intermittently switches between these different orbital states, yielding the emergence of multimodal statistics whose characteristic length scale is prescribed by the pilot-wavelength [17,21,25–28].

The second mechanism that may yield a statistical signature with the Faraday wavelength is the random-walk-like motion that has been reported in simulations exploring the long-path-memory limit of free [29] and confined walkers [30–32], in experimental investigations of walkers above the Faraday threshold [33], and walkers subjected to two-frequency excitation [34]. The random-walk dynamics is typically characterized by sustained periods during which the droplet is nearly stationary. The pilot wave then grows in amplitude until becoming sufficiently large to propel the droplet into an adjacent minimum of the pilot wave, at which point the process repeats itself. While the droplet motion is ballistic over short time-scales, the long-time statistical behaviour is diffusive [31,32]. A similar random-walk-like dynamics arises for walkers in a rotating frame, specifically *wobble-and-leap* motion [25,26], in which the droplet's orbital centre exhibits periods of near stasis before experiencing a rapid quantized leap in position. We here detail the origins of random-walk dynamics and the resulting statistical behaviour in the generalized pilot-wave framework.

Recent experimental and theoretical studies have suggested a third mechanism for generating a robust statistical signature with the Faraday wavelength, as arises due to the walker's response to disturbance. For sufficiently large vibrational forcing, when the droplet is perturbed from its free walking state, it may execute decaying in-line speed oscillations around the free walking speed [14] or large-amplitude periodic speed oscillations [35,36], both with a wavelength comparable to the Faraday wavelength. These speed oscillations may be generated when walkers interact with submerged topography [37]. For example, when a walker passes over a submerged well of relatively deep fluid, the resulting perturbation of the droplet speed induces in-line oscillations. In this setting, an ensemble of trajectories reveals a statistical signature with the Faraday wavelength comparable in form to Friedel oscillations [13]. Speed oscillations may also play a significant role when the droplet is confined to a corral [27,38], where the statistical signature of the droplet may be rationalized in terms of the correlation between position and speed arising due to speed oscillations prompted by droplet collisions with the outer boundary. We here assess the prevalence and importance of these oscillations in the context of a generalized pilot-wave framework.

We herein present a theoretical investigation of a classical pilot-wave system inspired by the similarities between the hydrodynamic pilot-wave system and de Broglie's mechanics. In §2, we define a generic classical pilot-wave system endowed with the common fundamental features of the walker system and de Broglie's mechanics. In §3, we systematically delineate the parameter regimes where perturbations to the steady propelled particle yield under- and over-damped in-line oscillations, and rationalize the correspondence between the oscillation length and the pilot-wavelength. Furthermore, we demonstrate that for sufficiently large wave forcing, the steady propulsion state destabilizes via a subcriticial Hopf bifurcation, leading to the emergence of either periodic or chaotic 'jittering' motion, in which the particle moves episodically. Chaotic jittering is shown to result in a random-walk-like motion. We explore the origins and statistical manifestations of this random-walk-like motion in §4. In §5, we discuss the manner in which our study informs the origins and ubiquity of the pilot-wavelength in the statistical signature of classical pilot-wave dynamics.

2. Pilot-wave dynamics

Inspired by the walking-droplet system [7], we consider an idealized system in two spatial dimensions in which a particle with position $\boldsymbol{x}_p(t)$ and mass m is guided by the slope of its accompanying pilot wave, and experiences a linear drag. The wave field is generated by the linear superposition of axisymmetric waves positioned along the particle's prior trajectory due to a periodic vibrational force, $F(t)$, exerted by the particle. This axisymmetric wave field is endowed with three defining properties known to be important in the walker system: the vertical oscillations resonate with the forcing $F(t)$; the waves are quasi-monochromatic with wavelength λ in the far field; and the waves decay exponentially over the time scale τ.

Table 1. The key dimensional and dimensionless parameters arising in our study.

	dimensional		dimensionless
m	particle mass	$\kappa_0 = m/D\tau_0$	particle mass
τ	wave dissipation rate	$\epsilon = \tau_0/\tau$	wave dissipation rate
τ_0	critical wave dissipation rate	$\Gamma = 1 - \epsilon$	path memory longevity
λ	pilot-wavelength	u	steady propulsion speed
A	wave amplitude	s_*	dominant eigenvalue
T	particle vibration period	$\omega = \mathrm{Im}[s_*]$	oscillation angular frequency
F_0	mean vibration force	$\Lambda = u/\omega$	normalized oscillation length
D	drag coefficient		

When the time scale of the particle's horizontal motion is long compared to the forcing period, T, time-averaging over one forcing period yields the stroboscopic trajectory equation for the particle's horizontal position $\boldsymbol{x}_p(t)$:

$$m\ddot{\boldsymbol{x}}_p + D\dot{\boldsymbol{x}}_p = -F_0\nabla h(\boldsymbol{x}_p, t), \tag{2.1}$$

where $h(\boldsymbol{x}, t)$ is the pilot-wave amplitude, F_0 is a mean coupling force and D is the drag coefficient [39]. Following this stroboscopic approximation, $h(\boldsymbol{x}, t)$ may be expressed as the integral over the particle's prior trajectory, namely

$$h(\boldsymbol{x}, t) = \frac{A}{T}\int_{-\infty}^{t} \mathcal{H}(k|\boldsymbol{x} - \boldsymbol{x}_p(s)|)\, \mathrm{e}^{-(t-s)/\tau}\, \mathrm{d}s, \tag{2.2}$$

where $k = 2\pi/\lambda$ and A is the stroboscopic amplitude of the wave generated by the particle [14]. In this idealized model, we neglect higher-order corrections to the wave form $\mathcal{H}$ arising in the walking-droplet system, such as travelling waves [9] and spatial damping [23,40–42]. While these effects are known to be important in multiple-droplet interactions [43–45], they have only a negligible influence on the propulsion of single droplets [39]. We, therefore, adopt the long-time quasi-monochromatic wave kernel $\mathcal{H}(r) = J_0(r)$ throughout this study, where J_0 is the Bessel function of the first kind of order zero [39]. Furthermore, for the sake of simplicity, we do not consider variations in the vibrational force $F(t)$, as may arise in the hydrodynamic system in response to changes in the local wave amplitude [43–46]. The fundamental property of this Newtonian pilot-wave system (2.1)–(2.2) is the self-generation of the guiding potential $h(\boldsymbol{x}, t)$. The temporal extent of the influence of the particle's prior trajectory is prescribed by the memory time, τ, a control parameter of the system that sets the longevity of the pilot-wave field.

When the drag force dominates the propulsive wave force, the particle's rest state $\dot{\boldsymbol{x}}_p = \boldsymbol{0}$ is stable and the accompanying pilot wave is axisymmetric about the particle. As the memory time, τ, is increased, the magnitude of the wave field in the stationary state scales with τ, leading to an increase of the wave force. Beyond a critical threshold,

$$\tau > \tau_0 = \sqrt{\frac{2DT}{F_0Ak^2}},$$

the stationary state destabilizes, symmetry is broken, and the particle is propelled at a constant speed in an arbitrary direction [7,14]. The parameters appearing in this critical threshold are defined in table 1, along with the dimensionless parameters to be developed in what follows.

To characterize the propulsion dynamics, we introduce the dimensionless variables $\hat{\boldsymbol{x}} = k\boldsymbol{x}$, $\hat{\boldsymbol{x}}_p = k\boldsymbol{x}_p$, $\hat{h} = hT/A\tau_0$ and $\hat{t} = t/\tau_0$. Upon substituting into (2.1)–(2.2) and dropping the carets, we obtain

the dimensionless pilot-wave system

$$\kappa_0 \ddot{x}_p + \dot{x}_p = -2\nabla h(\boldsymbol{x}_p, t) \tag{2.3a}$$

and

$$h(\boldsymbol{x}, t) = \int_{-\infty}^{t} J_0(|\boldsymbol{x} - \boldsymbol{x}_p(s)|)\, \mathrm{e}^{-\epsilon(t-s)}\, \mathrm{d}s, \tag{2.3b}$$

where the dimensionless parameters $\epsilon = \tau_0/\tau > 0$ and $\kappa_0 = m/D\tau_0 > 0$ describe the decay rate of the waves and the relative importance of the inertial and drag effects, respectively [10,47]. The dimensionless pilot-wave system (2.3) is the parametric generalization of the stroboscopic walking-droplet model of Oza *et al.* [14] originally proposed by Bush [10]. We characterize the longevity of the path memory through the parameter $\Gamma = 1 - \epsilon$, which increases from zero at the onset of propulsion to one in the long-path-memory limit, and may thus seen to be equivalent to the normalized vibrational forcing in the hydrodynamic system [10,47]. Of particular interest is the $\kappa_0 \to 0$ limit, in which the inertial effects are confined to rapid transients and the dynamics become dominated by gradient-driven motion, which, in this particular respect, is reminiscent of de Broglie's guidance equation. By contrast, walkers typically arise for $\kappa_0 \approx 1$, specifically $0.6 \lesssim \kappa_0 \lesssim 1.2$ in the parameter regimes thus far explored experimentally [16].

As the steady propulsion of the particle is neutrally stable to perturbations perpendicular to the line of motion [14], the essential physics of speed oscillations may be captured through consideration of the dynamics of a particle confined to a line. By writing $\boldsymbol{x}_p(t) = x_p(t)\boldsymbol{j}$, where $\boldsymbol{j}$ is an arbitrary horizontal unit vector, the pilot-wave system (2.3) may be combined as a dimensionless integro-differential equation

$$\kappa_0 \ddot{x}_p + \dot{x}_p = 2\int_{-\infty}^{t} J_1\left(x_p(t) - x_p(s)\right) \mathrm{e}^{-\epsilon(t-s)}\, \mathrm{d}s, \tag{2.4}$$

whose dynamics will be the subject of our investigation. The dimensionless speed, $u > 0$, of the particle's steady propulsion may be found by substituting the ansatz $x_p(t) = ut$ into (2.4) and solving for u. This free particle speed may be expressed in terms of either the path memory parameter, Γ, or the decay rate of the pilot wave, ϵ [14]:

$$u = \frac{1-\Gamma}{2}\left[-4 + \left(-1 + \sqrt{1 + 8(1-\Gamma)^{-2}}\right)^2\right]^{1/2} = \frac{1}{\sqrt{2}}\left(4 - \epsilon^2 - \epsilon\sqrt{\epsilon^2 + 8}\right)^{1/2}. \tag{2.5}$$

The free particle speed increases monotonically from zero at the propulsion threshold ($\Gamma = 0$), attaining a finite value $u = \sqrt{2}$ in the long-path-memory limit ($\Gamma = 1$).

3. Resonant oscillations with the anomalous pilot wave

To elucidate the origins of the particle's speed oscillations, we perform an analysis of the system's response to in-line perturbations from its steady self-propelling state. Our study reveals the existence of periodic velocity oscillations whose oscillation length is comparable to the pilot-wavelength.

(a) Asymptotic linear stability analysis of the particle's self-propulsion

Following the methodology of Oza *et al.* [14], we consider a small velocity perturbation to (2.4) of the form

$$\kappa_0 \ddot{x}_p + \dot{x}_p = 2\int_{-\infty}^{t} J_1(x_p(t) - x_p(s))\, \mathrm{e}^{-\epsilon(t-s)}\, \mathrm{d}s + \eta\delta(t), \tag{3.1}$$

where $\delta(t)$ is the Dirac delta function and $0 < |\eta| \ll 1$. For steady propulsion prior to the perturbation, we express the particle's trajectory as $x_p(t) = ut + \eta x_1(t)H(t)$, where $H(t)$ is the

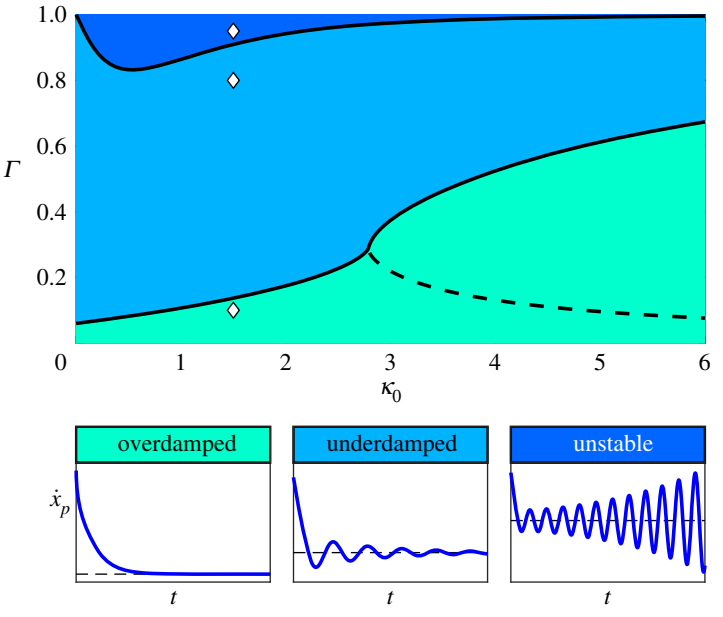

Figure 1. Regime diagram delineating the response of the steady self-propelling particle to small perturbations in its direction of motion, as predicted by the dominant asymptotic growth rate, s_*, computed from equation (3.3). As Γ is progressively increased, the response transitions from over- to under-damped oscillations, before destabilizing at sufficiently high values of Γ for all $\kappa_0 > 0$. The dashed curve denotes the onset of subdominant oscillations. The diamond markers determine the parameter values corresponding to the velocity evolution in the legend, namely $\kappa_0 = 1.5$ with $\Gamma = 0.10$, 0.80 and 0.95. (Online version in colour.)

Heaviside function. By expanding the nonlinear term in (3.1) to $O(|\eta|)$, the perturbed particle position, $x_1(t)$, evolves according to

$$\kappa_0 \ddot{x}_1 + \dot{x}_1 = \epsilon x_1 - 2\int_0^t x_1(t-s) J_1'(us)\, \mathrm{e}^{-\epsilon s}\, \mathrm{d}s, \tag{3.2}$$

where the initial conditions $x_1(0) = 0$ and $\dot{x}_1(0) = \kappa_0^{-1}$ follow from (3.1). The terms on the right-hand side of (3.2) may be interpreted as propulsive forces imparted by both the particle's deviation relative to the steady wave field (which simplifies to give ϵx_1) and perturbations to the pilot wave itself (corresponding to the integral term). Our analysis reveals that this anomalous wave field plays a fundamental role in determining the nature of the particle's response to perturbations.

We recast (3.2) in terms of the Laplace transform $X(s) = \mathcal{L}[x_1(t)](s)$ (for $s \in \mathbb{C}$ with $\mathrm{Re}[s+\epsilon] > 0$), where

$$X(s) = \left(\kappa_0 s^2 + s - \epsilon + 2\mathcal{L}\left[J_1'(ut)\, \mathrm{e}^{-\epsilon t}\right](s)\right)^{-1}.$$

The poles, $s \in \mathbb{C}$, of $X(s)$ determine the asymptotic exponential growth rates of (3.2) and satisfy

$$\kappa_0 s^2 + s - \epsilon + \frac{2(s+\epsilon)}{u^2(\epsilon)}\left[1 - \frac{s+\epsilon}{\sqrt{(s+\epsilon)^2 + u^2(\epsilon)}}\right] = 0. \tag{3.3}$$

We proceed to recast (3.3) as a polynomial in s of degree six, whose roots are candidate solutions to (3.3) [14]. Across the parameter regime considered in this study, (3.3) admits four roots, one of which is the root $s_0 = 0$ corresponding to translational invariance. We define s_* as the growth rate with maximum real part (discounting the root s_0), whose behaviour we characterize in figure 1.

Just beyond the propulsion threshold, the dominant growth rate is real and negative for all κ_0, indicating that any small perturbation to the steady propulsion speed will decay monotonically to zero [14,48,49]. As Γ is increased, two real roots of (3.3) collide in the complex plane and

form a complex-conjugate pair, resulting in the onset of oscillatory solutions to (3.2). For $\kappa_0 \lesssim 2.8$, this collision involves the dominant real growth rate, marking a bifurcation from overdamped to underdamped oscillations. By contrast, the complex-conjugate pair remains subdominant for $\kappa_0 \gtrsim 2.8$, and overdamped oscillations persist (as denoted by the dashed curve in figure 1). As Γ is further increased, the decay time of the underdamped oscillations increases and eventually surpasses that of the overdamped oscillations, yielding a qualitative change in the long-time response to perturbations. The change between these two qualitatively different transitions to underdamped oscillations results in the kink in the boundary curve evident in figure 1.

Within the regime of overdamped oscillations, the system's decay time increases with Γ until perturbations become neutrally stable (precisely, when $\mathrm{Re}[s_*] = 0$), a feature not reported by Oza *et al.* [14]. This onset of instability has also been observed in simulations of steady walkers in the long-path-memory limit [29,36]. In this unstable regime, perturbations to the particle's steady propulsion speed will grow until nonlinear effects, whose form we elucidate in §4, become significant (see the electronic supplementary material). From the asymptotic analysis of the instability threshold presented in appendix A, we find that the critical wave damping, $\epsilon = \epsilon_c \equiv 1 - \Gamma_c$, satisfies $\epsilon_c \sim \frac{2}{3}\kappa_0$ for $\kappa_0 \ll 1$, indicating that steady propulsion is unconditionally stable in the small-inertia limit $\kappa_0 \to 0$. When inertial effects dominate ($\kappa_0 \gg 1$), the instability threshold instead satisfies $\epsilon_c \sim \kappa_0^{-3}$. By combining the asymptotic results with the numerical solution presented in figure 1, we conclude that steady propulsion destabilizes for all $\kappa_0 > 0$, provided that the path memory is sufficiently long.

(b) The particle's oscillation length

While one may characterize these underdamped oscillations in terms of their dimensionless angular frequency, $\omega = \mathrm{Im}[s_*]$, it is instructive here to consider the evolution of the velocity as a function of the distance travelled by the particle, a feature not considered by Oza *et al.* [14]. In dimensionless variables, the ratio, Λ, of the oscillation length relative to the pilot-wavelength is related to the speed, u, and angular frequency, ω, via $\Lambda = u/\omega$. For walkers (with $\kappa_0 \approx 0.9$), the experiments of Wind-Willassen *et al.* [35] and Bacot *et al.* [36] demonstrated that this relative oscillation length, Λ, is close to unity.

In figure 2, we present the relative oscillation length predicted by the linear stability analysis of the steady self-propelling particle. In the small-inertia limit, the oscillation length deviates below the pilot-wavelength by up to 15%, with $\Lambda \to \sqrt{3}/2 \simeq 0.87$ as $\kappa_0 \to 0$ along the neutral stability curve (see appendix A for details). By contrast, the oscillation length remains within 2% of the pilot-wavelength for large κ_0. In particular, along the neutral stability curve the relative oscillation length satisfies $\Lambda \sim \sqrt{1 + (2\kappa_0^2)^{-1}}$ for $\kappa_0 \gg 1$, decreasing towards unity as $\kappa_0 \to \infty$. However, for intermediate κ_0, the contour along which the two lengths precisely coincide (highlighted in black in figure 2) does not correspond to an obvious physical limit. In order to deepen our understanding of this phenomenon, we explore the balance of forces arising during the particle's response to perturbation.

For a root $s \in \mathbb{C}$ of (3.3), we define the magnitude of the inertial, drag and wave forces as

$$\mathcal{I}(s) = |\kappa_0 s^2|, \quad \mathcal{D}(s) = |s| \quad \text{and} \quad \mathcal{W}(s) = |\kappa_0 s^2 + s|,$$

respectively. Moreover, we define the relaxation time-scale $\mathcal{T}(s) = 1/|\mathrm{Re}[s]|$. For sufficiently large Γ, (3.3) admits one real root, s_r, and a pair of complex-conjugate roots, s_c and s_c^*. We proceed to investigate how the force balance in these qualitatively different cases of over- and under-damped oscillations changes as κ_0 is varied (with Γ fixed). For notational efficiency, we will employ the abbreviation $\mathcal{I}_r = \mathcal{I}(s_r)$, and so forth.

In figure 3, we observe that the relaxation time-scale, $\mathcal{T}_r$, increases with increasing κ_0 (for Γ fixed), whereas $\mathcal{T}_c$ has a sharp peak for $\kappa_0 \approx 0.5$ (corresponding to the minimum in Γ_c, as seen in figure 1) before settling towards a constant value as κ_0 is increased. The change from underdamped to overdamped oscillations (with increasing κ_0) occurs when $\mathcal{T}_r = \mathcal{T}_c$,

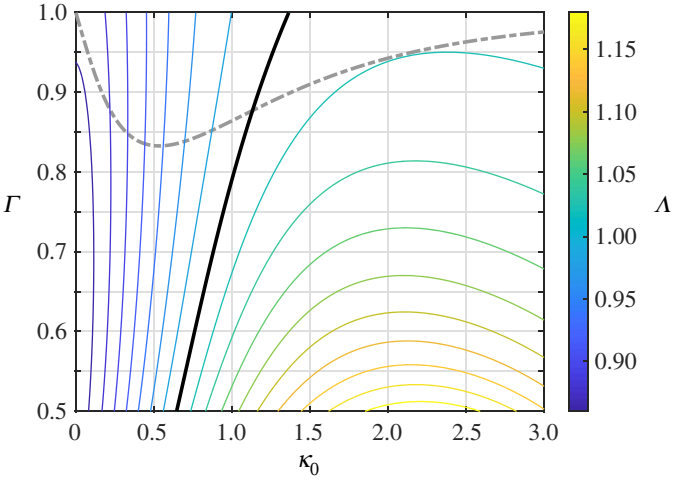

Figure 2. Contours of the relative oscillation wavelength, Λ, predicted by the linear stability analysis of the steady self-propelling state. The dash-dotted curve denotes the instability threshold (figure 1), while the contour $\Lambda = 1$ is highlighted in black. For smaller values of Γ (not shown), Λ sharply increases near the boundary between under- and over-damped oscillations. (Online version in colour.)

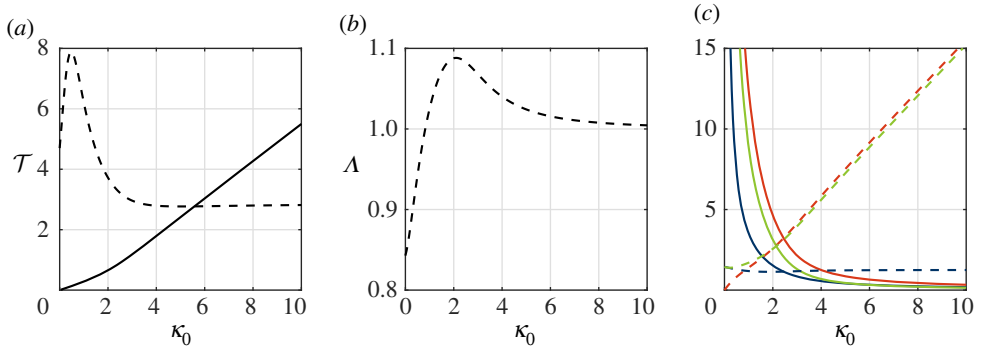

Figure 3. Characterization of the self-propelled particle's response to in-line perturbations when the asymptotic growth rate $s_* \in \mathbb{C}$ is real (s_r, solid curves) or part of a complex-conjugate pair (s_c, dashed curves), with $\Gamma = 0.65$ (which is characteristic of $\Gamma \gtrsim 0.3$). (*a*) Decay time-scale, $\mathcal{T}$, for stable oscillations for s_r and s_c. (*b*) Relative oscillation length, Λ, defined only for s_c. (*c*) The magnitude of the inertial $\mathcal{I}$ (orange), drag $\mathcal{D}$ (dark blue) and wave $\mathcal{W}$ (light green) forces for s_r and s_c. (Online version in colour.)

corresponding to $\kappa_0 \approx 5.6$ for $\Gamma = 0.65$. For overdamped oscillations (in both the dominant and subdominant regimes), we note that $\mathcal{T}_r$ depends linearly on κ_0 for $\kappa_0 \ll 1$ and $\kappa_0 \gg 1$. Since $\mathcal{T}_r = |s_r|^{-1}$, we obtain that $\mathcal{I}_r$, $\mathcal{D}_r$ and $\mathcal{W}_r$ all have size of $O(\kappa_0^{-1})$ for both $\kappa_0 \ll 1$ and $\kappa_0 \gg 1$: All three forces make a similar contribution to the response of the particle to overdamped oscillations (figure 3*c*).

In contrast, underdamped oscillations correspond to a markedly different force balance. Although underdamped oscillations are subdominant for large κ_0, we note that the oscillation length approaches the pilot-wavelength, as they do along the neutral stability curve. The near constant nature of $\mathcal{T}_c$ and Λ for large κ_0 indicates that s_c itself varies little in the complex plane. This observation is in accordance with $\mathcal{D}_c$ being nearly constant for large κ_0, while $\mathcal{I}_c$ increases linearly. The wave force must then provide a force balance, explaining why $\mathcal{W}_c$ also increases

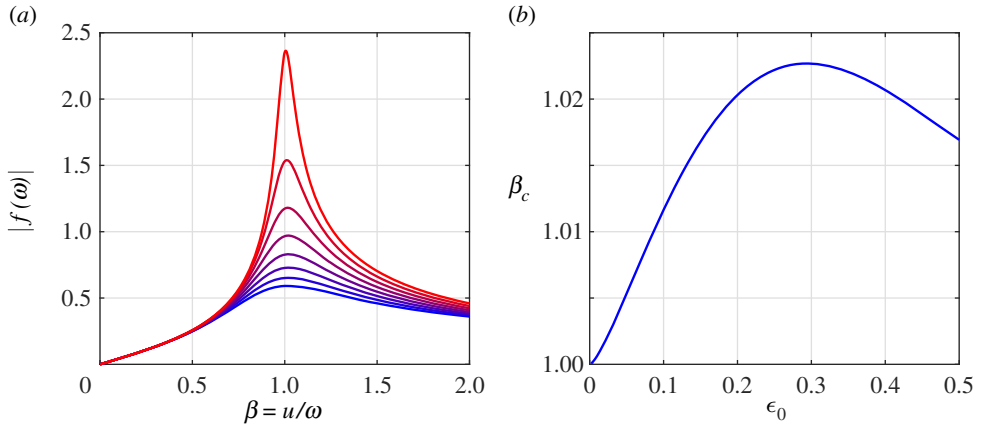

Figure 4. The magnitude of the propulsive kick supplied by the perturbation wave field, with $f(\omega)$ defined in (3.4) and $\epsilon = 0.35$ ($\Gamma = 0.65$). (*a*) The dependence of $|f(\omega)|$ on $\beta = u/\omega$, where $|f|$ becomes increasingly peaked as the effective damping ϵ_0 decreases from 0.4 (blue curve) to 0.05 (red curve) in decrements of 0.05. (*b*) The maximizer, β_c, of $|f|$, as a function of ϵ_0. (Online version in colour.)

nearly linearly with κ_0. As highlighted in figure 3*c*, when $\kappa_0 \gg 1$, drag effects are negligible and the dominant balance is between the inertial and wave forces.

To explain why this inertial-wave force balance results in the oscillation length approaching the pilot-wavelength for $\kappa_0 \gg 1$, we consider the contribution of the perturbation wave field (the integral term in (3.2)) to the particle's response to perturbations. When the particle's perturbation takes the asymptotic form $x_1(t) = C_0 e^{(\nu_0 + i\omega)t} + \text{c.c.}$ (where $C_0 \in \mathbb{C}$, $\nu_0 = \text{Re}[s_c]$, and c.c. denotes complex conjugation), the long-time contribution of the anomalous wave force is $C_0 e^{(\nu_0+i\omega)t} f(\omega) + \text{c.c.}$, where

$$f(\omega) = \int_0^\infty J_1'(ut)\, e^{-(\epsilon_0+i\omega)t}\, dt = \frac{(\epsilon_0 + i\omega)}{u^2}\left[1 - \frac{\epsilon_0 + i\omega}{\sqrt{(\epsilon_0 + i\omega)^2 + u^2}}\right], \tag{3.4}$$

and $\epsilon_0 = \nu_0 + \epsilon > 0$ is the effective damping. From the oscillatory nature of $J_1'(r)$ with asymptotic period 2π, we expect resonance between the terms $e^{-i\omega t}$ and $J_1'(ut)$ when u and ω approximately coincide. By fixing u and then treating ϵ_0 and ω as parameters, we explore the magnitude $|f(\omega)|$ in figure 4*a*. As ϵ_0 decreases towards zero, the function $|f(\omega)|$ exhibits an increasingly sharp maximum near $u/\omega = 1$, corresponding to a relative oscillation length close to unity.

Returning to the results of the linear stability analysis in the case of a complex-conjugate growth rate s_c, we deduce that the only way in which the balance $W_c \sim I_c \sim \kappa_0$ may arise for $\kappa_0 \gg 1$ is for the oscillation length to approach the pilot-wavelength. In accordance with figure 4*b*, the wave force may be maximized when u is slightly larger than ω, explaining why the pilot-wavelength is attained from above as $\kappa_0 \to \infty$. While the underdamped oscillations eventually become subdominant to the overdamped oscillations in the large-inertia limit, this resonant oscillation appears to be fundamental in the pilot-wave dynamics. In particular, given that the relative oscillation length is less than unity for $\kappa_0 \ll 1$ and tends to unity from above for $\kappa_0 \gg 1$, continuity requires that the relative oscillation length must be unity for an intermediate value of κ_0, coinciding with the regime of walkers explored by Wind-Willassen *et al.* [35] and Bacot *et al.* [36].

(c) Periodic oscillations and the origins of a subcritical Hopf bifurcation

To rationalize the pilot-wave dynamics close to the instability threshold, we develop a method for seeking periodic velocity oscillations [35,36] to the trajectory equation (2.4). Bacot *et al.*

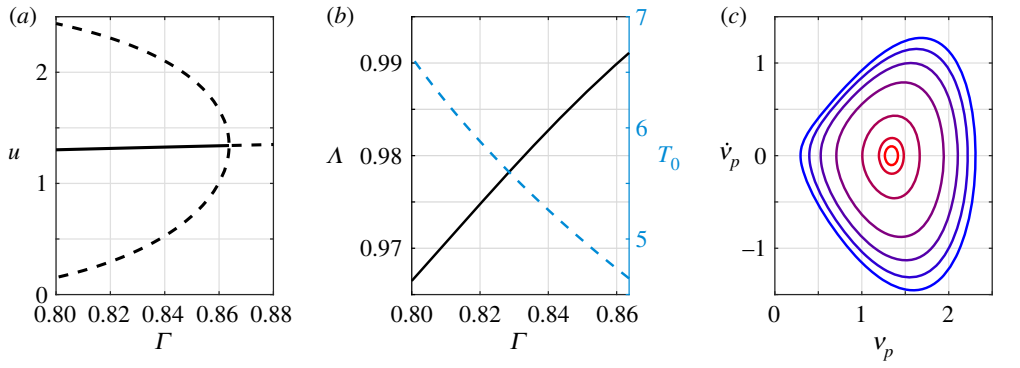

Figure 5. Evidence of the subcritical Hopf bifurcation for $\kappa_0 = 1$ and $\Gamma_c \simeq 0.8637$. (*a*) The stable dimensionless self-propulsion speed (solid curve) and the velocity bounds of the unstable limit cycle (dashed curves) as a function of Γ. (*b*) The relative oscillation length Λ (black curve) and the dimensionless oscillation period T_0 (blue curve) of the unstable limit cycle for $\Gamma < \Gamma_c$. (*c*) Sample trajectories in dimensionless velocity-acceleration phase space for selected values of Γ in the range $\Gamma = 0.82$ (blue) to $\Gamma = 0.8635$ (red), where $v_p = \dot{x}_p$. (Online version in colour.)

[36] reported the coexistence of droplets walking at a constant speed, with either periodic velocity oscillations or chaotic behaviour. Similar periodic velocity variations are predicted by the stroboscopic model close to the instability threshold. In order to systematically identify the periodic solutions and their stability, we proceed quasi-analytically by positing a Fourier series ansatz for the particle's horizontal velocity with period T_0, as is outlined in appendix B. The stability of the periodic velocity oscillations is assessed by direct numerical simulation of the trajectory equation (2.4), with an imposed prior trajectory corresponding to the periodic solution so obtained. The spectral method used to simulate (2.4) is detailed in appendix C.

Our computations reveal that small-amplitude velocity oscillations emerge below the instability threshold ($\Gamma < \Gamma_c$) for all $\kappa_0 > 0$, yet are unstable. Figure 5 details the dependence of the amplitude of the velocity oscillations on the path memory for a characteristic value of the inertia coefficient, namely $\kappa_0 = 1$. For $\Gamma \sim 0.8$, the variation in the amplitude of the oscillation is of the same order as the velocity itself. As Γ is increased towards the instability threshold ($\Gamma < \Gamma_c$), the amplitude of the velocity oscillations rapidly decreases, so that the unstable limit cycle vanishes precisely at the instability threshold. This behaviour is representative of a *subcritical* Hopf bifurcation, implying that just beyond the instability threshold ($\Gamma > \Gamma_c$), stable small-amplitude velocity oscillations do not generally exist and the system instead approaches a distant attractor. Moreover, the relative oscillation length, Λ, approximately coincides with unity (as shown in figure 5*b*), again underscoring the prevalence of the pilot-wavelength, λ, in the dynamics of a free particle.

Unlike the prototypical example of a subcritical Hopf bifurcation, a saddle-node bifurcation of cycles (from which a large-amplitude stable limit cycle arises [50]) does not arise along the bifurcation branch subtending from the subcritical Hopf bifurcation. The dynamics arising along this bifurcation branch will be explored elsewhere. Extensive simulation of the pilot-wave dynamics in the regime where the walking state is stable ($\Gamma < \Gamma_c$) did not reveal evidence of any additional periodic states.

4. Jittering modes and their statistical manifestation

We proceed to explore the second mechanism for the emergence of quantized statistical behaviour, random-walk-like motion arising in the parameter regime where steady propulsion is unstable. Following a perturbation from the self-propelling state, oscillations in the particle's velocity grow in magnitude, eventually leading to a reversal in the particle's direction of motion. When the

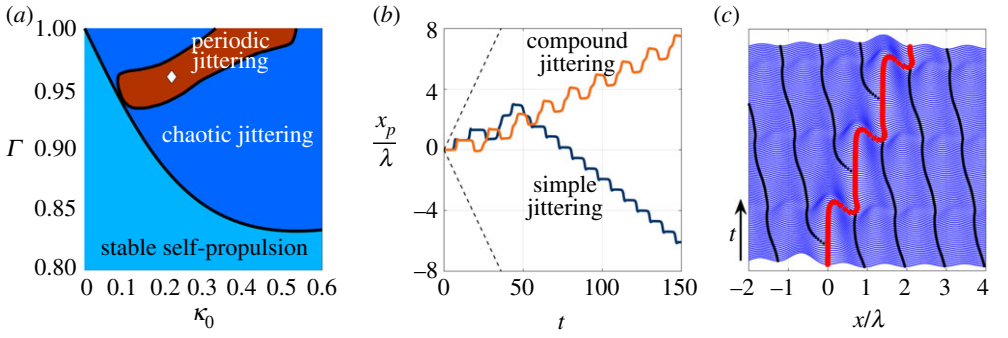

Figure 6. The dynamics of jittering modes. (*a*) Regime diagram delineating the emergence of jittering modes. Light blue denotes the regime in which the steady self-propelling state is stable. Above the black curve ($\Gamma > \Gamma_c$), this steady self-propulsion gives way to jittering modes. Red denotes the region in which stable periodic jittering modes (either simple or compound) arise. Dark blue indicates regions where both steady self-propulsion and periodic jittering are unstable, and chaotic jittering emerges. The white diamond indicates the parameter values used in panels (*b*) and (*c*), namely $\kappa_0 = 0.22$ and $\Gamma = 0.96$. (*b*) Coexistence of stable periodic jittering modes. The system was initialized with $x_p = 0$, $v_p = v_0$ and $h = 0$, with initial dimensionless particle velocity $v_0 = 10^{-3}$ for simple jittering (blue curve) and $v_0 = 10^{-5}$ for compound jittering (orange curve). For both simple and compound periodic jittering modes, periodic motion is achieved after an initial transient. The period of the compound jittering is approximately twice that of the simple jittering. The slope of the black dashed lines corresponds to the steady propulsion speed u, and highlights the relatively slow mean speed of the jittering modes. (*c*) The pilot wave (blue) and particle position (red dots) over three oscillation periods for the simple jittering mode depicted in panel (*b*). Black squares denote the minima of the pilot-wave field. (Online version in colour.)

particle's motion is confined to a line, periodic and chaotic velocity oscillations may persist: the particle's velocity remains close to zero for a sustained period of time, during which the pilot wave builds up beneath the particle. This growth concludes when the wave force dominates the drag force, and the particle is rapidly propelled to one of the neighbouring minima of the pilot wave, at which point the system relaxes and the velocity is quickly damped due to the confining action of the wave field. This growth-relaxation process can be seen in the periodic 'jittering' modes portrayed in figure 6 and the electronic supplementary material. Similar dynamics have been previously observed in numerical simulations of walkers in the limit of vanishing inertia [31,32] and in the long-path-memory limit [29,30], resulting in motion akin to a random walk.

Figure 6*a* indicates the dependence of the system behaviour on κ_0 and Γ. The light blue region indicates the parameter regime in which steady self-propulsion is stable ($\Gamma < \Gamma_c$). Above the black curve, we delineate the emergence of jittering modes, characterized by stable periodic jittering (red region) and chaotic jittering (dark blue region). Both regions were found via simulation of (2.4) using the spectral method described in appendix C. Within the periodic jittering regime, we observe both simple periodic jittering modes, in which the jitter direction remains constant, and compound jittering, in which the jitter direction alternates, but asymmetry in the left-right motion results in a net drift. We also observe multistability of simple and compound jittering: both states may be accessed at the same (κ_0, Γ) from different initializations (see figure 6*b*). When κ_0 is increased (and with it, particle inertia), trapping of the particle by a neighbouring minimum of the pilot wave may be achieved only in the limit $\Gamma \to 1$. Periodic jittering modes are not observed in the regime in which steady propulsion is stable: the neutral stability curve defines the extent of periodic jittering modes. We note that, as in the hydrodynamic regime [30], periodic oscillations of the particle's position about a fixed point in space appear to be unstable.

We proceed to rationalize the underlying mechanics of these jittering modes and assess their prevalence in classical pilot-wave systems via consideration of the system's ensemble statistics.

(a) The mechanics of jittering modes

Due to the near-symmetry of the pilot wave about the particle during the growth stage and the large speed (up to three times the steady propulsion speed) of the particle during the relaxation stage, the dynamics in the relaxation stage may be approximated by that of a damped particle moving in a static potential $\mathcal{V}(x) = aJ_0(x - x_0)$, which is an approximation to the wave field generated during the growth stage and local to the particle. The amplitude, a, of this self-generated potential [51] is determined by the longevity of the growth stage and the decay rate of the waves, ϵ. The displacement, x_0, may be approximated by an averaged position of the particle during the growth phase. The particle then evolves according to the temporally local differential equation $\kappa_0\ddot{x}_p + \dot{x}_p = -\mathcal{V}'(x_p)$ until it reaches a neighbouring minimum of $\mathcal{V}(x)$ and local wave growth recommences. For small κ_0, the oscillations about the minimum of the potential occur on a fast time-scale, yielding an approximation to gradient-driven motion.

To gain insight into the growth stage of the jittering modes, we consider a model problem in which the particle is initialized with a small horizontal velocity and an undisturbed pilot wave. In the early stages of the particle's trajectory, we assume that $|x_p(t) - x_p(s)| \ll 1$ for all $0 < s < t$, allowing us to reduce (2.4) to the linearized integro-differential equation

$$\kappa_0\ddot{x}_p + \dot{x}_p = \int_0^t \left(x_p(t) - x_p(s)\right) \mathrm{e}^{-\epsilon(t-s)}\, \mathrm{d}s, \tag{4.1}$$

with initial conditions $x_p(0) = x_0$ (which is arbitrary, due to translational invariance) and $\dot{x}_p(0) = v_0$. For (4.1) to be a valid approximation of (2.4) over $O(1)$ time-scales, we require $|v_0| \ll 1$. As derived in appendix D, the velocity of the particle, $v_p(t) = \dot{x}_p(t)$, evolves according to

$$v_p(t) = \exp\left(-\frac{1 + \kappa_0\epsilon}{2\kappa_0}t\right)\left(c_1 J_\nu\left(\gamma \mathrm{e}^{-\epsilon t/2}\right) + c_2 Y_\nu\left(\gamma \mathrm{e}^{-\epsilon t/2}\right)\right), \tag{4.2}$$

where $\gamma = 2/\sqrt{\epsilon^3\kappa_0}$, and $J_\nu(z)$ and $Y_\nu(z)$ are Bessel functions of the first and second kind, respectively, with order

$$\nu = \frac{1}{\epsilon^{3/2}\kappa_0}\sqrt{4\kappa_0 + \epsilon(1 - \epsilon\kappa_0)^2}.$$

The constants c_1 and c_2 are determined by the initial conditions $v_p(0) = v_0$ and $\dot{v}_p(0) = -v_0/\kappa_0$.

To compare the long-time dynamics of this reduced model (4.2) with the growth stage of the jittering modes predicted by the full nonlinear model (2.4), we first approximate the asymptotic growth of the particle's normalized velocity by

$$V(t) = \frac{Y_\nu\left(\gamma \mathrm{e}^{-\epsilon t/2}\right)}{Y_\nu(\gamma)} \exp\left(-\frac{1 + \kappa_0\epsilon}{2\kappa_0}t\right), \tag{4.3}$$

where $V(0) = 1$ and $v_p/V \to c_2 Y_\nu(\gamma)$ as $t \to \infty$. The dependence of $V(t)$ on the parameters κ_0 and ϵ is characterized in figure 7. Despite the complicated form of (4.3), the behaviour is relatively simple: the growth of V occurs on a faster time scale when either κ_0 is decreased or ϵ is decreased. As portrayed in figure 7*c*, the function $CV(t - t_*)$ gives excellent agreement to the simulated particle velocity, $v_p(t)$, for the growth stage of periodic jittering modes, where the amplification, C, and time shift, t_*, are chosen to match the onset of the growth stage. This reduced model also accurately describes the growth stage in the regime of chaotic jittering, which is characterized by unpredictable changes in the particle's direction and significant variations in the particle's velocity, as presented in figure 8 and the electronic supplementary material. Upon segmenting a long trajectory into its periods of growth (denoted by the orange highlights in figure 8*b*), the relative velocity of all these sub-trajectories collapse onto the curve $V(t)$. This result highlights that the linearized model (4.1) contains all of the essential physics required to characterize the growth stage, despite the nonlinearity and complexity of the pilot-wave system (2.4).

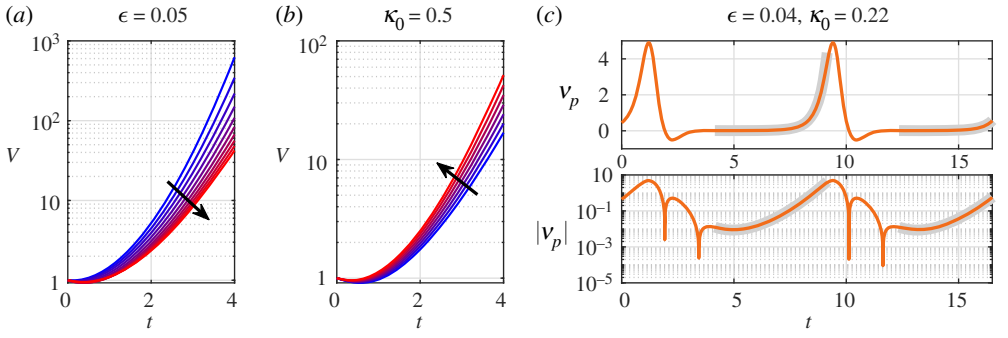

Figure 7. Evolution of the function $V(t)$ defined in (4.3). (*a*) $\epsilon = 0.05$ fixed with κ_0 increasing (denoted by the arrow) from 0.05 (blue) to 0.5 (red) in increments of 0.05. (*b*) $\kappa_0 = 0.5$ fixed with ϵ decreasing (denoted by the arrow) from 0.20 (blue) to 0.02 (red) in decrements of 0.03. (*c*) Comparison of the simulated dimensionless velocity $v_p(t)$ (orange curves) and the growth stage prediction $CV(t - t_*)$ (grey curves) for periodic jittering modes for $\epsilon = 0.04$ and $\kappa_0 = 0.22$, where C and t_* are judiciously chosen. The same data is presented in both the upper and lower panels. (Online version in colour.)

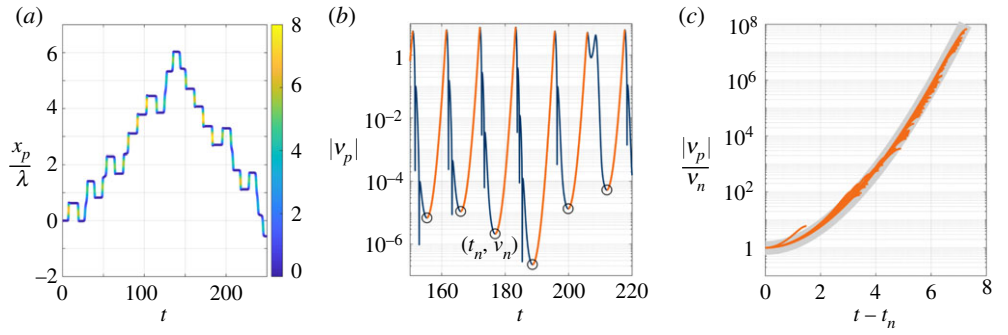

Figure 8. Chaotic jittering modes, with $\kappa_0 = 0.1$ and $\Gamma = 0.97$. (*a*) The evolution of the particle's dimensionless position, x_p. The trajectory is colour coded according to the particle's dimensionless speed. (*b*) The particle's dimensionless speed with sub-trajectories corresponding to the growth stage of the jittering mode highlighted in orange. The black circles denote the onset of growth at time t_n with speed $v_n = |v_p(t_n)|$. (*c*) Collapse of the normalized sub-trajectories (orange) onto the curve $V(t - t_*)$ (grey), where the additional shift $t_* = 0.1$ ensures that the speed minima coincide. (Online version in colour.)

(b) From coherent to incoherent ensemble statistics

We proceed by exploring the evolution of an ensemble of nearly identically prepared systems in the regime of chaotic jittering, where both steady propulsion and periodic jittering modes are unstable (denoted by the dark blue region in figure 6*a*). We thus demonstrate the emergence of wavelike statistical structure at short times and diffusive behaviour at long times. Specifically, we consider $N_0 = 10^6$ realizations of (2.4), where each particle is initialized at the origin with a vanishing accompanying pilot wave and a small, random initial velocity. Each particle immediately enters the growth stage, before jittering chaotically in a random-walk-like motion. As demonstrated in figure 9, the probability density function (PDF) initially exhibits sharp peaks spaced by a length scale comparable to the pilot-wavelength due to the near-constant step length of the random walk (corresponding to the neighbouring minimum of the accompanying pilot wave). However, small fluctuations in this step length accumulate over time until the peaks of the PDF become obscured.

To characterize this long-time behaviour, we consider the evolution of the mean-squared displacement $\Delta(t) = N_0^{-1} \sum_{n=1}^{N_0} x_n^2(t)$, where $x_n(t)$ is the particle position in the nth realization.

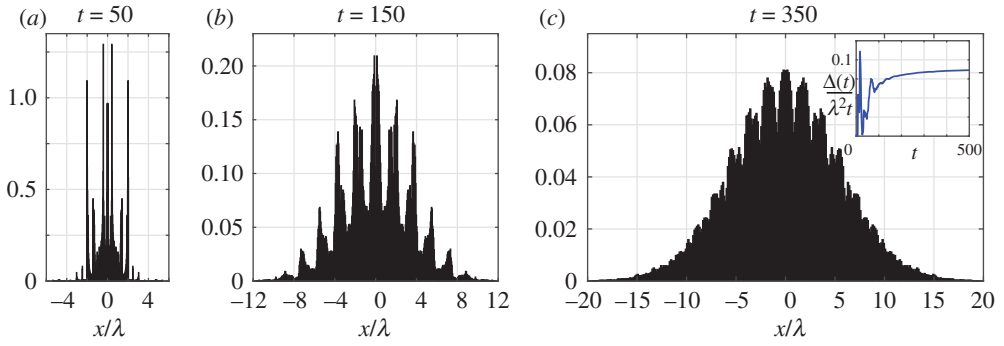

Figure 9. Evolution of the probability density function (PDF) for an ensemble of 10^6 particles initialized at the origin with a mean-zero normally distributed initial velocity with a dimensionless variance of 10^{-6}. The accompanying pilot wave for each realization is zero initially. The system parameters are $\kappa_0 = 0.25$ and $\Gamma = 0.90$, corresponding to the regime of chaotic jittering. The PDF is portrayed at dimensionless times (*a*) $t = 50$, (*b*) $t = 150$, and (*c*) $t = 350$. The inset denotes the evolution of $\Delta(t)/(\lambda^2 t)$ (where $\Delta(t)$ is the mean-squared displacement), which appears to approach a constant as $t \to \infty$, indicating asymptotic diffusion. (Online version in colour.)

As highlighted in the inset of figure 9*c*, the quantity $\Delta(t)/(\lambda^2 t)$ initially oscillates (due to the random-walk-like motion) before approaching a constant value in the limit $t \to \infty$, indicating asymptotic diffusion. Simulations revealed that the diffusion coefficient decreases monotonically with increasing Γ, a trend that might be anticipated on the grounds that larger amplitude waves are expected to more efficiently trap the particle. The diffusion coefficient generally increases with κ_0, indicating that particle inertia enhances diffusion; however, the relation between the two is not strictly monotonic. Further investigation of the influence of Γ and κ_0 on the effective diffusivity is left for future consideration.

To rationalize the transition from coherent statistics, characterized by a PDF with sharp peaks, to those in which the asymptotic PDF is Gaussian-like, we analyse the evolution of a toy model for the chaotic jittering modes. For simplicity, we neglect memory effects and fluctuations in the time between steps. Specifically, we consider a stochastic, discrete-time, Markovian jump process, where the particle can move left or right at each timestep with equal probability, yet the distance travelled fluctuates about the mean, $\mu > 0$, with variance $\sigma^2 > 0$. We describe each displacement in terms of the PDF, $P(x)$, given as a Gaussian mixture model

$$P(x) = \frac{1}{\sqrt{2\pi\sigma^2}}\left[\frac{1}{2}\exp\left(-\frac{(x-\mu)^2}{2\sigma^2}\right) + \frac{1}{2}\exp\left(-\frac{(x+\mu)^2}{2\sigma^2}\right)\right].$$

At each timestep, n, the PDF of the particle's position, $p_n(x)$, is then expressed as the convolution

$$p_{n+1}(x) = \int_{-\infty}^{\infty} P(x-x')p_n(x')\,\mathrm{d}x' = (P * p_n)(x).$$

We consider the case in which the initial distribution, $p_0(x)$, is symmetric about $x = 0$. Despite the simplicity of this toy model, we proceed to show that this jump process exhibits a transition to asymptotic diffusion qualitatively similar to that evident in our simulations of (2.4).

By defining the Fourier transforms $\hat{p}_n(\xi)$ and $\hat{P}(\xi)$ of $p_n(x)$ and $P(x)$, respectively, successive applications of the convolution theorem yield $\hat{p}_n = \hat{P}^n\hat{p}_0$. Inversion back to physical space gives

$$p_n(x) = \frac{1}{2\pi}\int_{-\infty}^{\infty} \cos^n(\xi\mu)\mathrm{e}^{-n\sigma^2\xi^2/2}\mathrm{e}^{-\mathrm{i}\xi x}\hat{p}_0(\xi)\,\mathrm{d}\xi.$$

At short times, $p_n(x)$ exhibits several sharp peaks, qualitatively similar to figure 9*a*. The long-time ($n \to \infty$) evolution of the PDF is approximated by means of Laplace's method, giving

$$p_n(x) \approx \frac{1}{\sqrt{2\pi n\sigma_0^2}} \exp\left(-\frac{x^2}{2n\sigma_0^2}\right),$$

where $\sigma_0^2 = \sigma^2 + \mu^2$, indicating that the random variable describing the asymptotic displacement obeys a normal distribution with mean zero and variance $n\sigma_0^2$. The evolution of $p_n(x)$ is presented in the electronic supplementary material. In the context of the pilot-wave dynamics with mean step period T_p, the asymptotic diffusion coefficient is $\mathcal{D}_0 = \sigma_0^2/2T_p$. Furthermore, by writing $T_p = \mu/u_0$ for the mean speed u_0 and using the approximations $\sigma \ll \mu \sim \lambda$, we deduce that the asymptotic diffusion coefficient obeys the scaling $\mathcal{D}_0 \sim u_0\lambda$.

5. Discussion

We have characterized two mechanisms for the emergence of quantized statistical patterns from classical pilot-wave dynamics [10], specifically in-line speed oscillations and the random walks associated with chaotic jittering modes. Both mechanisms are rooted in structured oscillations of the particle speed, with a length scale prescribed by the wavelength of the pilot wave. Our study provides new theoretical rationale for the speed oscillations and emergent statistical structure reported in several experimental and theoretical investigations of pilot-wave hydrodynamics, and suggests the prevalence of such behaviour in a broader class of pilot-wave systems.

With a view to understanding the roots of the speed oscillations prompted by perturbations to the particle's free self-propelling state, we presented a detailed linear stability analysis thereof. The particle may respond to perturbations with either underdamped or overdamped oscillations. In the case of underdamped oscillations, the oscillation wavelength is comparable to the pilot-wavelength. In the small-inertia limit, where the wave force is balanced by the drag force, the relative oscillation length is slightly less than unity. In the large-inertia limit, a regime previously unexplored in classical pilot-wave settings, the relative oscillation length approaches unity from above. In the finite-inertia regime of the hydrodynamic pilot-wave system [16], the relative oscillation length is approximately unity [36]. In this hydrodynamic limit, the underdamped in-line speed oscillations provide a robust mechanism for the emergence of a statistical footprint with the wavelength of the pilot wave, as has been reported in a number of settings [13,27,37,38].

Our study has also revealed the form of the onset of instability of the particle's steady self-propelling state in this generalized pilot-wave framework. Via a numerical study of a parameter regime in the vicinity of the instability threshold, we demonstrated the existence of a subcritical Hopf bifurcation. For our system, this bifurcation does not give rise to coexisting stable steady self-propulsion and large-amplitude periodic velocity oscillations, as was observed in experimental studies of the hydrodynamic pilot-wave system [35,36]. We note that consideration of physical effects not described by our generic pilot-wave model, such as the finite contact time of the droplet and its pilot-wave field [36] and variations in the droplet's vertical dynamics [35,40,45], may be necessary to capture such dynamical behaviour.

As a further consequence of this subcritical Hopf bifurcation, just beyond the instability threshold, stable, small-amplitude limit cycles are not obtained; instead, jittering modes emerge. These jittering modes are characterized by sustained periods in which the particle is nearly stationary and the pilot wave grows in magnitude until the particle is rapidly propelled into a neighbouring trough of its pilot wave. While a parameter regime characterized by periodic jittering was identified, chaotic jittering was more prevalent when the steady self-propelling state was unstable. For one-dimensional motion, at short times, chaotic jittering results in random-walk-like behaviour and an associated multimodal PDF of the particle position. At long times, the dynamics may be characterized by the diffusivity $\mathcal{D}_0 \sim u_0\lambda$, where u_0 is the mean speed of the particle. We recall Nelson's [6] assertion that quantum mechanics may be seen as a diffusive process with diffusivity $\mathcal{D}_0 = \hbar/(2m) \sim U\lambda_B$, where $U = \hbar k_B/m$ is the particle speed and $\lambda_B = 2\pi/k_B$

the de Broglie wavelength. Hence, our study reveals that, in the chaotic jittering regime, classical pilot-wave dynamics takes the form of a random walk akin to Nelson's description of quantum mechanics [6]. Precisely characterizing the dependence of the diffusion coefficient, $\mathcal{D}_0$, on the system parameters κ_0 and Γ in this generic pilot-wave system will be the subject of future work. Particular attention will be given to characterizing the evolution of the system's ensemble statistics and comparing this evolution to the predictions of the standard quantum formalism.

While figure 9 elucidates the manner in which chaotic jittering leads to multimodal statistical structure for one-dimensional motion, it is less clear how such statistical structure might arise for motion in the plane. It is possible that the emergence of coherent statistics for two-dimensional motion relies on the influence of the boundaries. For example, Gilet's [32] simulations of a walker in a circular cavity in the zero-particle-inertia and infinite-memory limit, showed that similar chaotic jittering took the form of the particle alternating between preferred radii prescribed by the form of the dominant cavity modes. The particle motion was diffusive, and the diffusion coefficient took a form similar to $\mathcal{D}_0 \sim u_0\lambda$. Unlike in our system, however, the mean-squared displacement saturated at finite time due to the confinement of the particle. The random-walk-like motion between preferred radii ultimately gave rise to the emergence of a coherent wavelike statistical distribution. While the pilot-wave dynamics and statistics presented in experimental studies of the hydrodynamic corral [27,38] differ considerably from those of Gilet's model [32], structured speed oscillations are prevalent in both systems, and provide a mechanism for the emergence of multimodal long-time statistics.

It is valuable here to discuss the relation between the jittering modes elucidated here in our idealized pilot-wave system and various dynamical states reported in experimental studies of the hydrodynamic pilot-wave system. While chaotic jittering modes have not been reported for free walking droplets, our study suggests that they would be most likely to arise at a reduced vibrational frequency in the small-droplet, high-memory limit, as was inferred by Oza *et al.* [16] as the region most likely to support hydrodynamic spin states. We note, however, that a droplet's vertical motion is typically chaotic in the limit of high vibrational forcing [35,39], an effect that might conceivably give rise to destructive interference of the wave field beneath the droplet, potentially destabilizing the jittering state. Chaotic motion akin to jittering has been reported in the long-path-memory limit of the walker system when the droplet is confined to a circular corral [28]. Similar jittering behaviour has also been observed above the Faraday threshold, a regime in which the droplet navigates a background field of Faraday waves, and exhibits asymptotic diffusion [33]. Likewise, irregular episodic motion has been reported for subcritical, two-frequency vibrational forcing [34]. Finally, the wobble-and-leap dynamics of a walker in a rotating frame [25,26] may be understood in terms of a jittering state tempered by system rotation.

In the theoretical framework explored here, the particle is propelled by the slope of the pilot wave generated by its periodic vibration. One could in principle consider other forms of wave-particle coupling, such as those considered in quantum pilot-wave models. In Bohmian mechanics [52,53], the particle is propelled by gradients of the quantum potential, whose form may be deduced from the wave function solution to the Schrödinger equation. In the double-solution pilot-wave theory of de Broglie [1–3], the particle velocity is proportional to the gradient of the phase of a monochromatic pilot wave that evolves according to the Klein–Gordon equation. Notably, if the pilot wave is monochromatic and the field is real, the gradient of the phase is proportional to the slope of the wave.

From the perspective of workers in classical pilot-wave dynamics, the principal shortcoming of the quantum pilot-wave theories is the absence of a mechanism for particle-induced wave generation [54]. This shortcoming has motivated a pair of recent models of quantum dynamics inspired and informed by the walker system. Andersen *et al.* [55] explored a model in which the pilot wave is generated by localized periodic particle excitation of the Schrödinger equation, and considered the particle velocity as being proportional to the gradient of the wave phase. In the hydrodynamic quantum field theory (HQFT) of Dagan & Bush [56], the authors explore a variant of de Broglie's original formulation: the particle velocity is proportional to the slope of the pilot wave generated by localized periodic particle excitation of the Klein–Gordon equation.

While the possibilities for alternative wave-particle couplings are numerous, we expect the in-line speed oscillations elucidated here to be a generic feature of pilot-wave systems with a quasi-monochromatic guiding field; indeed, such speed oscillations have already been seen to emerge in HQFT [56].

As a caveat, we emphasize that the generalized pilot-wave model examined here has limitations in terms of capturing all the richness of the hydrodynamic pilot-wave system, owing to the neglect of certain physical effects, such as spatial damping of the pilot wave [9,23,40–42] and modulations in the particle's vertical dynamics [35,40,45]. Likewise, we note the possibility that additional unforeseen physical effects, such as a stochastic background field, may serve to enhance, alter or suppress in-line oscillations and random walks in microscopic pilot-wave systems [10].

Data accessibility. The code supporting this article has been uploaded as part of the electronic supplementary material.

Authors' contributions. J.W.M.B. proposed the study. The analysis was performed by M.D. and S.E.T. The paper was written by all three authors. All authors gave final approval for publication and agree to be held accountable for the work performed therein.

Competing interests. We declare we have no competing interests.

Funding. The authors gratefully acknowledge the NSF for financial support through grant no. CMMI-1727565.

Acknowledgements. The authors thank Pedro J. Séenz and Rodolfo Rosales for insightful discussions.

Appendix A. Asymptotic analysis of the instability threshold

We proceed to investigate the nature of the neutral stability curve, along which the dominant roots of (3.3) have the form $s_* = \pm \mathrm{i}\omega$ for $\omega \in \mathbb{R}$ (where $\omega > 0$ without loss of generality). By fixing κ_0, the dimensionless critical damping, $\epsilon = \epsilon_c$, and angular frequency, ω, satisfy

$$-\kappa_0\omega^2 + \mathrm{i}\omega - \epsilon_c + \frac{2}{u_c^2}(\mathrm{i}\omega + \epsilon_c)\left(1 - \frac{\mathrm{i}\omega + \epsilon_c}{\sqrt{u_c^2 - \omega^2 + \epsilon_c^2 + 2\mathrm{i}\omega\epsilon_c}}\right) = 0, \tag{A 1}$$

where $u_c = u(\epsilon_c)$. We analyse the solutions to (A 1) for $\epsilon_c \ll 1$. For tractable analysis, we simplify the term $\sqrt{u_c^2 - \omega^2 + \epsilon_c^2 + 2\mathrm{i}\omega\epsilon_c}$ by assuming

$$\epsilon_c\sqrt{\epsilon_c^2 + 4\omega^2} \ll |u_c^2 - \omega^2|, \tag{A 2}$$

from which we use the approximation $(1+z)^{-1/2} \sim 1 - \frac{1}{2}z$ for $|z| \ll 1$. We consider the cases $u_c > \omega$ and $u_c < \omega$ separately, which we find correspond to the limits $\kappa_0 \gg 1$ and $\kappa_0 \ll 1$, respectively. Following, the conclusion of each calculation, we verify that (A 2) is indeed satisfied. In the following calculations, we use the following approximation of the critical propulsion speed, u_c, for $\epsilon_c \ll 1$ (where $u_c = u(\epsilon_c)$ is defined in (2.5)), namely

$$u_c^2 \sim 2 - \sqrt{2}\epsilon_c + O(\epsilon_c^2). \tag{A 3}$$

(a) Case $u_c > \omega > 0$

This case corresponds to the relative oscillation length $\Lambda > 1$, from which we rationalize the instability for $\kappa_0 \gg 1$. By applying assumption (A 2), the real and imaginary parts of (A 1) yield

$$-\kappa_0\omega^2 - \epsilon_c + \frac{2}{u_c^2}\left(\epsilon_c + \frac{\omega^2 - \epsilon_c^2}{\sqrt{u_c^2 - \omega^2}} + \frac{\epsilon_c^2}{2}\frac{\epsilon_c^2 - 5\omega^2}{(u_c^2 - \omega^2)^{3/2}}\right) = 0 \tag{A 4a}$$

and

$$1 + \frac{2}{u_c^2}\left(1 - \frac{2\epsilon_c}{\sqrt{u_c^2 - \omega^2}} + \epsilon_c\frac{2\epsilon_c^2 - \omega^2}{(u_c^2 - \omega^2)^{3/2}}\right) = 0. \tag{A 4b}$$

To proceed, we define $\omega = \alpha u_c$, where $\alpha \in (0,1)$ is a real parameter of size $O(1)$, which is to be determined from the following analysis. Using (A 3) to expand u_c^2 in powers of ϵ_c, we express (A 4) in terms of the two unknowns, ϵ_c and α, yielding

$$\kappa_0\left(\epsilon_c - \sqrt{2}\right) + \frac{1}{\sqrt{1-\alpha^2}}\left(1 + \frac{\epsilon_c}{2\sqrt{2}}\right) = O(\epsilon_c^2) \tag{A 5a}$$

and

$$2 + \frac{\epsilon_c}{\sqrt{2}}\left(1 - \frac{2}{\sqrt{1-\alpha^2}} - \frac{\alpha^2}{(1-\alpha^2)^{3/2}}\right) = O(\epsilon_c^2). \tag{A 5b}$$

Re-arranging (A 5*a*) yields

$$\frac{1}{\sqrt{1-\alpha^2}} = \kappa_0\left(\sqrt{2} - \frac{3}{2}\epsilon_c + O(\epsilon_c^2)\right), \tag{A 6}$$

whereby neglecting the $O(\epsilon_c^2)$ terms and substituting into (A 5*b*) gives the following approximation for the stability threshold:

$$\epsilon_c \sim \frac{2\sqrt{2}}{\sqrt{2}\kappa_0(1+2\kappa_0^2) - 1}.$$

To satisfy $\epsilon_c \ll 1$, we require $\kappa_0 \gg 1$, yielding the leading-order approximation $\epsilon_c \sim \kappa_0^{-3}$. Neglecting the $O(\epsilon_c)$ terms in (A 6) yields the approximation

$$\alpha = \frac{\omega}{u_c} \sim \sqrt{1 - \frac{1}{2\kappa_0^2}},$$

where α is the reciprocal relative oscillation length. Hence, the oscillation length decreases towards the pilot-wavelength for large κ_0. To justify assumption (A 2), we substitute in the computed values of ω and u_c in terms of κ_0 into (A 2). After some algebra, we find that $\epsilon_c\sqrt{\epsilon_c^2 + 4\omega^2}/|u_c^2 - \omega^2| \sim 2\sqrt{2}\kappa_0^{-1}$, from which we deduce that (A 2) is indeed valid for $\kappa_0 \gg 1$.

(b) Case $\omega > u_c > 0$

This second case corresponds to the relative oscillation length $\Lambda < 1$, which we use to rationalize the instability for $\kappa_0 \ll 1$. By applying assumption (A 2), the real and imaginary parts of (A 1) determine

$$-\kappa_0\omega^2 - \epsilon_c + \frac{2\epsilon_c}{u_c^2}\left(1 - \frac{2\omega}{\sqrt{\omega^2 - u_c^2}} + \frac{\omega^3 - 2\omega\epsilon_c^2}{(\omega^2 - u_c^2)^{3/2}}\right) = 0 \tag{A 7a}$$

and

$$\omega + \frac{2}{u_c^2}\left(\omega + \frac{\epsilon_c^2 - \omega^2}{\sqrt{\omega^2 - u_c^2}} + \frac{\epsilon_c^2}{2}\frac{\epsilon_c^2 - 5\omega^2}{(\omega^2 - u_c^2)^{3/2}}\right) = 0. \tag{A 7b}$$

As before, we define $\omega = \alpha u_c$, where $\alpha > 1$ is a real parameter of size $O(1)$, which is to be determined from the following analysis. By applying the approximation (A 3) of u_c^2 for $\epsilon_c \ll 1$, equation (A 7*a*) yields

$$-\frac{2\kappa_0\alpha^2}{\epsilon_c}\left(1 + O(\epsilon_c)\right) - 1 + \left(1 + O(\epsilon_c)\right)\left(1 - \frac{2\alpha}{\sqrt{\alpha^2 - 1}} + \frac{\alpha^3}{(\alpha^2-1)^{3/2}} + O(\epsilon_c^2)\right) = 0. \tag{A 8}$$

For the correct dominant balance when $\epsilon_c \ll 1$, we require $\kappa_0 = \kappa_1\epsilon_c$ (where $\kappa_1 = O(1)$ is an unknown constant), implying that $\kappa_0 \ll 1$. By neglecting terms of $O(\epsilon_c)$ in (A 8), we obtain

$$2\kappa_1\alpha \sim \frac{\alpha^2}{(\alpha^2-1)^{3/2}} - \frac{2}{\sqrt{\alpha^2-1}}. \tag{A 9}$$

Similarly, by substituting (A 3) in (A 7*b*) and neglecting terms of $O(\epsilon_c^2)$, we find that

$$2 \sim \frac{\alpha}{\sqrt{\alpha^2 - 1}} + \frac{\epsilon_c}{\sqrt{2}} \quad \Longrightarrow \quad \alpha \sim \frac{2}{\sqrt{3}}\left(1 + \frac{\epsilon_c}{6\sqrt{2}}\right). \tag{A 10}$$

Substituting (A 10) into (A 9) gives $\kappa_1 = \frac{3}{2} + O(\epsilon_c)$. Hence, the stability threshold satisfies $\epsilon_c \sim \frac{2}{3}\kappa_0$ for $\kappa_0 \ll 1$, and the corresponding reciprocal relative oscillation length is

$$\alpha \sim \frac{2}{\sqrt{3}}\left(1 + \frac{\kappa_0}{9\sqrt{2}}\right) \quad \text{for } \kappa_0 \ll 1.$$

To validate assumption (A 2) in this case, we compute $\epsilon_c\sqrt{\epsilon_c^2 + 4\omega^2}/|u_c^2 - \omega^2| \sim 4\sqrt{\frac{2}{3}}\kappa_0$, from which we deduce that (A 2) is indeed valid for $\kappa_0 \ll 1$.

Appendix B. Computing periodic velocity oscillations

To compute periodic velocity oscillations of the dimensionless trajectory equation (2.4) with unknown period T_0, we introduce the rescaled time variable $\hat{t} = \omega_0 t$ (where $\omega_0 = 2\pi/T_0$). Substitution into (2.4) and dropping the carets yields

$$\kappa_0 \ddot{x}_p + \frac{1}{\omega_0}\dot{x}_p = \frac{2}{\omega_0^3}\int_0^\infty J_1\big(x_p(t) - x_p(t-s)\big)\mathrm{e}^{-\epsilon s/\omega_0}\,\mathrm{d}s. \tag{B 1}$$

We now seek 2π-periodic solutions for $\dot{x}_p$, namely

$$\dot{x}_p(t) = \frac{a_0}{2} + \sum_{n=1}^{\infty} a_n \cos(nt) + b_n \sin(nt), \tag{B 2}$$

where the unknown Fourier coefficients a_n and b_n are real. By temporal invariance, we are free to choose a condition on the velocity at $t = 0$: without loss of generality, we set $\ddot{x}_p(0) = 0$, supplying the requirement

$$\sum_{n=1}^{\infty} n b_n = 0, \tag{B 3}$$

which provides a condition for the unknown oscillation period T_0 (or equivalently, ω_0).

Upon substituting (B 2) into the trajectory equation (B 1) and using orthogonality, we obtain the following system of equations for the Fourier coefficients a_n and b_n:

$$\kappa_0 n b_n + \frac{a_n}{\omega_0} - \frac{2}{\omega_0^3\pi}\int_0^{2\pi} I(t)\cos(nt)\,\mathrm{d}t = 0, \quad \forall\, n \geq 0 \tag{B 4a}$$

and

$$-\kappa_0 n a_n + \frac{b_n}{\omega_0} - \frac{2}{\omega_0^3\pi}\int_0^{2\pi} I(t)\sin(nt)\,\mathrm{d}t = 0, \quad \forall\, n \geq 1, \tag{B 4b}$$

where we define the 2π-periodic function $I(t) = \int_0^\infty \mathrm{e}^{-\epsilon s/\omega_0} J_1(\chi(t,s))\,\mathrm{d}s$ in terms of the difference in the particle's position, $\chi(t,s)$, defined as

$$\chi(t,s) = \frac{a_0}{2}s + \sum_{n=1}^{\infty}\frac{a_n}{n}\Big(\sin(nt) - \sin(n(t-s))\Big) - \frac{b_n}{n}\Big(\cos(nt) - \cos(n(t-s))\Big).$$

The periodicity of the integrands in equations (B 4) allows for quadrature with spectral accuracy, while the integral $I(t)$ is evaluated using an adaptive Gauss-Kronrod quadrature method built into Matlab. For fixed κ_0 and ϵ, we then truncate the Fourier series to the first N frequencies, leaving $2N + 2$ unknowns, specifically $\{T_0, a_0, \ldots, a_N, b_1, \ldots, b_N\}$, which satisfy that $2N + 2$ equations given by (B 3)–(B 4). We solve the system using Newton's method, where $N = 12$ Fourier modes is sufficient to resolve the periodic trajectories in the vicinity of $\epsilon = \epsilon_c$.

Appendix C. Numerical simulation of the trajectory equation

We implement a spectral method to efficiently evolve the pilot-wave system (2.4). For time $t<0$, we impose a prescribed trajectory $x_p(t)=x_0(t)$, where $x_0(0)=0$ without loss of generality. Owing to the translational invariance of the system, we define $H(x,t)$ as the cross section of the wave field along the particle's line of motion expressed in the frame of reference of the particle. Consequently, (2.4) may be recast as the system

$$\kappa_0\ddot{x}_p+\dot{x}_p=-2\frac{\partial H}{\partial x}(0,t) \tag{C 1a}$$

and

$$H(x,t)=\int_{-\infty}^{t}J_0(x+x_p(t)-x_p(s))\mathrm{e}^{-\epsilon(t-s)}\,\mathrm{d}s. \tag{C 1b}$$

Applying Neumann's Addition Theorem [57] to (C 1b) gives the decomposition $H(x,t)=H_0(t)J_0(x)+2\sum_{n=1}^{\infty}H_n(t)J_n(x)$, where

$$H_n(t)=(-1)^n\int_{-\infty}^{t}J_n(x_p(t)-x_p(s))\mathrm{e}^{-\epsilon(t-s)}\,\mathrm{d}s. \tag{C 2}$$

Using the identity $J_n'(x)=\frac{1}{2}(J_{n-1}(x)-J_{n+1}(x))$, we differentiate (C 2) to recast $H_n(t)$ as a series of coupled differential equations. We thus reformulate the pilot-wave system (C 1) as

$$\dot{x}_p=v_p, \tag{C 3a}$$

$$\kappa_0\dot{v}_p+v_p+2H_1=0, \tag{C 3b}$$

$$\dot{H}_0-v_pH_1+\epsilon H_0=1 \tag{C 3c}$$

and

$$\dot{H}_n-\frac{v_p}{2}\left(H_{n+1}-H_{n-1}\right)+\epsilon H_n=0,\quad \forall\, n\geq 1. \tag{C 3d}$$

We note that the nonlinearity in the system now appears in the coupling between coefficients $H_n(t)$. Equation (C 2) yields the initial conditions $H_n(0)=\int_{-\infty}^{0}J_n(x_0(s))\mathrm{e}^{\epsilon s}\,\mathrm{d}s$ for all $n\geq 0$.

For numerical implementation, we set $H_n\equiv 0$ for all $n>N_*$, where the integer N_* specifies the accuracy of the solution. To determine a suitable value for N_*, we consider the steady propulsion state in which $x_p(t)=ut$ (where u is given in (2.5)) and the wave field coefficients, H_n, are time-independent. It follows from (C 2) that $H_n=\rho\Theta^n$, where $\rho=(\epsilon^2+u^2)^{-1/2}$ and $\Theta=\left(\epsilon-\sqrt{\epsilon^2+u^2}\right)/u$. To satisfy $|H_{N_*}|<\delta_0$ for some prescribed tolerance $\delta_0>0$, we require

$$N_*>\frac{\log\delta_0-\log\rho}{\log|\Theta|}.$$

A tolerance of $\delta_0=10^{-3}$ is satisfied by $N_*=5$ for $\Gamma=0.1$, $N_*=15$ for $\Gamma=0.5$, and $N_*=90$ for $\Gamma=0.9$. The time evolution of (C 3) is performed using a fourth-order Runge–Kutta method.

Appendix D. Analytic solution to the linearized trajectory equation

To reduce the integro-differential equation (4.1) to a temporally local differential equation, we differentiate (4.1) with respect to t to deduce that the particle's velocity, $v_p(t)=\dot{x}_p(t)$, satisfies

$$\kappa_0\ddot{v}_p+(1+\epsilon\kappa_0)\dot{v}_p+\frac{1}{\epsilon}\left(\epsilon^2-1+\mathrm{e}^{-\epsilon t}\right)v_p=0, \tag{D 1}$$

with initial conditions $v_p(0)=v_0$ and $\dot{v}_p(0)=-v_0/\kappa_0$ (where the latter condition is deduced from (4.1)). By defining $a=(\epsilon^{-1}-\epsilon)/\kappa_0$ and $b=\frac{1}{2}(\kappa_0^{-1}+\epsilon)$ for $0<\epsilon<1$ and $\kappa_0>0$, we recast (D 1) as

$$\frac{\mathrm{d}^2}{\mathrm{d}t^2}\left(\mathrm{e}^{bt}v_p(t)\right)+\left(\frac{\mathrm{e}^{-\epsilon t}}{\epsilon\kappa_0}-\left(a+b^2\right)\right)\mathrm{e}^{bt}v_p(t)=0.$$

By introducing the change of variables $z=\sqrt{4\mathrm{e}^{-\epsilon t}/\epsilon^3\kappa_0}$ with $G(z)=\mathrm{e}^{bt}v_p(t)$, we find that $G(z)$ satisfies Bessel's equation, $z^2G''(z)+zG'(z)+(z^2-\nu^2)G(z)=0$, with real order $\nu=2\epsilon^{-1}\sqrt{a+b^2}$.

The particle velocity is then

$$v_p(t) = \mathrm{e}^{-bt}\left(c_1 J_\nu\left(\gamma \mathrm{e}^{-\epsilon t/2}\right) + c_2 Y_\nu\left(\gamma \mathrm{e}^{-\epsilon t/2}\right)\right), \tag{D 2}$$

where $J_\nu(z)$ and $Y_\nu(z)$ are Bessel functions of the first and second kind, respectively, $\gamma = 2/\sqrt{\epsilon^3 \kappa_0}$, and the real constants c_1 and c_2 are determined by the initial conditions. The small-argument approximations $J_\nu(x) \propto x^\nu$ and $Y_\nu(x) \propto x^{-\nu}$ as $x \to 0$ [57] provide that the J_ν and Y_ν terms in (D 2) induce asymptotic exponential decay and growth, respectively.

References

1. de Broglie L. 1926 *Ondes et mouvements*. Paris, France: Gautier Villars.
2. de Broglie L. 1930 *An introduction to the study of wave mechanics*. London, UK: Methuen.
3. de Broglie L. 1987 Interpretation of quantum mechanics by the double solution theory. *Ann. Fond.* **12**, 1–23.
4. Gilder L. 2009 *The age of entanglement: when quantum physics was reborn*. New York City, NY: Vintage.
5. Bacciagaluppi G, Valentini A. 2009 *Quantum theory at the crossroads: reconsidering the 1927 Solvay conference*. Cambridge, UK: Cambridge University Press.
6. Nelson E. 1966 Derivation of the Schrödinger Equation from Newtonian Mechanics. *Phys. Rev.* **150**, 1079–1085. (doi:10.1103/PhysRev.150.1079)
7. Couder Y, Protière S, Fort E, Boudaoud A. 2005 Walking and orbiting droplets. *Nature* **437**, 208. (doi:10.1038/437208a)
8. Protière S, Boudaoud A, Couder Y. 2006 Particle-wave association on a fluid interface. *J. Fluid Mech.* **554**, 85–108. (doi:10.1017/S0022112006009190)
9. Eddi A, Sultan E, Moukhtar J, Fort E, Rossi M, Couder Y. 2011 Information stored in Faraday waves: the origin of a path memory. *J. Fluid Mech.* **674**, 433–463. (doi:10.1017/S0022112011000176)
10. Bush JWM. 2015 Pilot-wave hydrodynamics. *Annu. Rev. Fluid Mech.* **47**, 269–292. (doi:10.1146/annurev-fluid-010814-014506)
11. Bush JWM, Couder Y, Gilet T, Milewski PA, Nachbin A. 2018 Introduction to focus issue on hydrodynamic quantum analogs. *Chaos* **28**, 096001. (doi:10.1063/1.5055383)
12. Harris DM, Brun PT, Damiano A, Faria LM, Bush JWM. 2018 The interaction of a walking droplet and a submerged pillar: from scattering to the logarithmic spiral. *Chaos* **28**, 096105. (doi:10.1063/1.5031022)
13. Sáenz PJ, Cristea-Platon T, Bush JWM. 2020 A hydrodynamic analog of Friedel oscillations. *Sci. Adv.* **6**, eaay9234. (doi:10.1126/sciadv.aay9234)
14. Oza AU, Rosales RR, Bush JWM. 2013 A trajectory equation for walking droplets: hydrodynamic pilot-wave theory. *J. Fluid Mech.* **737**, 552–570. (doi:10.1017/jfm.2013.581)
15. Labousse M, Perrard S, Couder Y, Fort E. 2016 Self-attraction into spinning eigenstates of a mobile wave source by its emission back-reaction. *Phys. Rev. E* **94**, 042224. (doi:10.1103/PhysRevE.94.042224)
16. Oza AU, Rosales RR, Bush JWM. 2018 Hydrodynamic spin states. *Chaos* **28**, 096106. (doi:10.1063/1.5034134)
17. Tambasco LD, Bush JWM. 2018 Exploring orbital dynamics and trapping with a generalized pilot-wave framework. *Chaos* **28**, 096115. (doi:10.1063/1.5033962)
18. Valani RN, Slim A. 2018 Pilot-wave dynamics of two indentical, in-phase bouncing droplets. *Chaos* **28**, 096114. (doi:10.1063/1.5032128)
19. Fort E, Eddi A, Boudaoud A, Moukhtar J, Couder Y. 2010 Path-memory induced quantization of classical orbits. *Proc. Natl Acad. Sci. USA* **107**, 17 515–17 520. (doi:10.1073/pnas.1007386107)
20. Oza AU, Harris DM, Rosales RR, Bush JWM. 2014 Pilot-wave dynamics in a rotating frame: on the emergence of orbital quantization. *J. Fluid Mech.* **744**, 404–429. (doi:10.1017/jfm.2014.50)
21. Perrard S, Labousse M, Miskin M, Fort E, Couder Y. 2014 Self-organization into quantized eigenstates of a classical wave-driven particle. *Nature Commun.* **5**, 3219. (doi:10.1038/ncomms4219)
22. Labousse M, Oza AU, Perrard S, Bush JWM. 2016 Pilot-wave dynamics in a harmonic potential: quantization and stability of circular orbits. *Phys. Rev. E* **93**, 033122. (doi:10.1103/PhysRevE.93.033122)

23. Durey M, Milewski PA. 2017 Faraday wave-droplet dynamics: discrete-time analysis. *J. Fluid Mech.* **821**, 296–329. (doi:10.1017/jfm.2017.235)
24. Kurianski KM, Oza AU, Bush JWM. 2017 Simulations of pilot-wave dynamics in a simple harmonic potential. *Phys. Rev. Fluids* **2**, 113602. (doi:10.1103/PhysRevFluids.2.113602)
25. Harris DM, Bush JWM. 2014 Droplets walking in a rotating frame: from quantized orbits to multimodal statistics. *J. Fluid Mech.* **739**, 444–464. (doi:10.1017/jfm.2013.627)
26. Oza AU, Wind-Willassen Ø, Harris DM, Rosales RR, Bush JWM. 2014 Pilot-wave hydrodynamics in a rotating frame: exotic orbits. *Phys. Fluids* **26**, 082101. (doi:10.1063/1.4891568)
27. Harris DM, Moukhtar J, Fort E, Couder Y, Bush JWM. 2013 Wavelike statistics from pilot-wave dynamics in a circular corral. *Phys. Rev. E* **88**, 011001. (doi:10.1103/PhysRevE.88.011001)
28. Cristea-Platon T, Sáenz PJ, Bush JWM. 2018 Walking droplets in a circular corral: quantisation and chaos. *Chaos* **28**, 096116. (doi:10.1063/1.5034123)
29. Hubert M, Perrard S, Labousse M, Vandewalle N, Couder Y. 2019 Tunable bimodal explorations of space from memory-driven deterministic dynamics. *Phys. Rev. E* **100**, 032201. (doi:10.1103/PhysRevE.100.032201)
30. Durey M, Milewski PA, Bush JWM. 2018 Dynamics, emergent statistics, and the mean-pilot-wave potential of walking droplets. *Chaos* **28**, 096108. (doi:10.1063/1.5030639)
31. Gilet T. 2014 Dynamics and statistics of wave-particle interactions in a confined geometry. *Phys. Rev. E* **90**, 052917. (doi:10.1103/PhysRevE.90.052917)
32. Gilet T. 2016 Quantumlike statistics of deterministic wave-particle interactions in a circular cavity. *Phys. Rev. E* **93**, 042202. (doi:10.1103/PhysRevE.93.042202)
33. Tambasco LD, Pilgram JJ, Bush JWM. 2018 Bouncing droplet dynamics above the Faraday threshold. *Chaos* **28**, 096107. (doi:10.1063/1.5031426)
34. Sampara N, Gilet T. 2016 Two-frequency forcing of droplet rebounds on a liquid bath. *Phys. Rev. E* **94**, 053112. (doi:10.1103/PhysRevE.94.053112)
35. Wind-Willassen Ø, Moláček J, Harris DM, Bush JWM. 2013 Exotic states of bouncing and walking droplets. *Phys. Fluids* **25**, 082002. (doi:10.1063/1.4817612)
36. Bacot V, Perrard S, Labousse M, Couder Y, Fort E. 2019 Multistable free states of an active particle from a coherent memory dynamics. *Phys. Rev. Lett.* **122**, 104303. (doi:10.1103/PhysRevLett.122.104303)
37. Cristea-Platon T. 2019 Hydrodynamic analogues of quantum corrals and Friedel oscillations. PhD thesis, Massachusetts Institute of Technology, Cambridge, MA.
38. Sáenz PJ, Cristea-Platon T, Bush JWM. 2018 Statistical projection effects in a hydrodynamic pilot-wave system. *Nat. Phys.* **14**, 315–319. (doi:10.1038/s41567-017-0003-x)
39. Moláček J, Bush JWM. 2013 Drops walking on a vibrating bath: towards a hydrodynamic pilot-wave theory. *J. Fluid Mech.* **727**, 612–647. (doi:10.1017/jfm.2013.280)
40. Milewski PA, Galeano-Rios CA, Nachbin A, Bush JWM. 2015 Faraday pilot-wave dynamics: modelling and computation. *J. Fluid Mech.* **778**, 361–388. (doi:10.1017/jfm.2015.386)
41. Tadrist L, Shim JB, Gilet T, Schlagheck P. 2018 Faraday instability and subthreshold Faraday waves: surface waves emitted by walkers. *J. Fluid Mech.* **848**, 906–945. (doi:10.1017/jfm.2018.358)
42. Turton SE, Couchman MMP, Bush JWM. 2018 A review of the theoretical modeling of walking droplets: toward a generalized pilot-wave framework. *Chaos* **28**, 096111. (doi:10.1063/1.5032221)
43. Galeano-Rios CA, Couchman MMP, Bush JWM. 2018 Ratcheting droplet pairs. *Chaos* **28**, 096112. (doi:10.1063/1.5032116)
44. Oza AU, Siéfert E, Harris DM, Moláček J, Bush JWM. 2017 Orbiting pairs of walking droplets: dynamics and stability. *Phys. Rev. Fluids* **2**, 053601. (doi:10.1103/PhysRevFluids.2.053601)
45. Couchman MMP, Turton SE, Bush JWM. 2019 Bouncing phase variations in pilot-wave hydrodynamics and the stability of droplet pairs. *J. Fluid Mech.* **871**, 212–243. (doi:10.1017/jfm.2019.293)
46. Arbelaiz J, Oza AU, Bush JWM. 2018 Promenading pairs of walking droplets: dynamics and stability. *Phys. Rev. Fluids* **3**, 013604. (doi:10.1103/PhysRevFluids.3.013604)
47. Oza AU. 2014 A trajectory equation for walking droplets: hydrodynamic pilot-wave theory. PhD thesis, Massachusetts Institute of Technology, Cambridge, MA.
48. Bush JWM, Oza AU, Moláček J. 2014 The wave-induced added mass of walking droplets. *J. Fluid Mech.* **755**, R7. (doi:10.1017/jfm.2014.459)

49. Labousse M, Perrard S. 2014 Non-Hamiltonian features of a classical pilot-wave system. *Phys. Rev. E* **90**, 022913. (doi:10.1103/PhysRevE.90.022913)
50. Strogatz SH. 2001 *Nonlinear dynamics and chaos: with applications to physics, biology, chemistry and engineering*. Boulder, CO: Westview Press.
51. Nachbin A, Milewski PA, Bush JWM. 2017 Tunneling with a hydrodynamic pilot-wave model. *Phys. Rev. Fluids* **2**, 034801. (doi:10.1103/PhysRevFluids.2.034801)
52. Bohm D. 1952a A suggested interpretation of the quantum theory in terms of 'Hidden' variables. I. *Phys. Rev.* **85**, 166–179. (doi:10.1103/PhysRev.85.166)
53. Bohm D. 1952b A suggested interpretation of the quantum theory in terms of 'Hidden' variables. II. *Phys. Rev.* **85**, 180–193. (doi:10.1103/PhysRev.85.180)
54. Colin S, Durt T, Willox R. 2017 L. de Broglie's double solution program: 90 years later. *Annales de la Fondation Louis de Broglie* **42**, 19–71.
55. Andersen A, Madsen J, Reichelt C, Rosenlund Ahl S, Lautrup B, Ellegaard C, Levinsen MT, Bohr T. 2015 Double-slit experiment with single wave-driven particles and its relation to quantum mechanics. *Phys. Rev. E* **92**, 013006. (doi:10.1103/PhysRevE.92.013006)
56. Dagan Y, Bush JWM. 2020 Hydrodynamic quantum field theory: the free particle. *Comptes Rendus Mécanique*. Accepted.
57. Abramowitz M, Stegun I. 1964 *Handbook of mathematical functions*. Mineola, NY: Dover Publications.